



Ultracompact wavefront characterization of femtosecond 3D printed microlenses using double-frequency Ronchi interferometry

CLAUDIA IMIOLCZYK,^{1,*}  TERESA KLARA PFAU,¹ SIMON THIELE,²
JULIAN KARST,¹  MORITZ FLOESS,¹  MICHAEL SCHMID,¹ 
MARIO HENTSCHEL,¹  AND HARALD GIESSEN¹ 

¹4th Physics Institute and Research Center SCoPE, University of Stuttgart, Germany

²Institute of Technical Optics and Research Center SCoPE, University of Stuttgart, Germany

*claudia.imiolczyk@pi4.uni-stuttgart.de

Abstract: 3D printed microoptics have become important tools for miniature endoscopy, novel CMOS-based on-chip sensors, OCT-fibers, among others. Until now, only image quality and spot diagrams were available for optical characterization. Here, we introduce Ronchi interferometry as ultracompact and quick quantitative analysis method for measuring the wavefront aberrations after propagating coherent light through the 3D printed miniature optics. We compare surface shapes by 3D confocal microscopy with optical characterizations by Ronchi interferograms. Phase retrieval gives us the transversal wave front aberration map, which indicates that the aberrations of our microlenses that have been printed with a Nanoscribe GT or Quantum X printer exhibit RMS wavefront aberrations as small as $\lambda/20$, Strehl ratios larger than 0.91, and near-diffraction limited modulation transfer functions. Our method will be crucial for future developments of 3D printed microoptics, as the method is ultracompact, ultra-stable, and very fast regarding measurement and evaluation. It could fit directly into a 3D printer and allows for in-situ measurements right after printing as well as fast iterations for improving the shape of the optical surface.

Published by Optica Publishing Group under the terms of the [Creative Commons Attribution 4.0 License](https://creativecommons.org/licenses/by/4.0/). Further distribution of this work must maintain attribution to the author(s) and the published article's title, journal citation, and DOI.

1. Introduction

Femtosecond 3D printing has advanced tremendously since its inception in 1999 [1]. Microoptical elements that include spherical, aspherical, doublet and triplet, diffractive, refractive-diffractive, and achromatic or even apochromatic elements have been demonstrated [2–11]. Applications such as microlens arrays [12–15], fiber collimation and coupling, refractive and holographic beam shaping, laser beam collimation, OAM generation, optical trapping, and optical coherence tomography [16–30] have been enabled and improved by this method.

In most cases, quality control of such microoptical elements include confocal surface measurements, 3D and confocal microscopy [31–33], as well as far-field mode and imaging quality. Often, MTFs are being measured by imaging USAF test targets and determining contrast of the different elements in the varying groups.

However, in order to truly quantify the optical performance of a system, it is not enough to characterize only the surface, but the entire transmitted wavefront aberration should be quantified. The reason is that inhomogeneities in the 3D printed polymer due to local refractive index variations and internal strain can add to the aberrations [7], in addition to deviations of the surface shape from the desired optical design.

Often, wavefront aberrations are quantified using Mach-Zehnder or Twyman-Green interferometers [34]. However, these setups are often bulky, quite alignment sensitive, and require

sufficient stability to avoid accidental phase shifts on the order of $\lambda/4$ or more. These prerequisites prohibit their integration into 3D printers, which would require ultracompact optical setups, insensitivity to alignment, and stable operation. If a quick turnaround from a measurement to an improved surface shape is required, the measurement and phase front evaluation time should also be minimal. Often, these setups are not suited for microoptics due to the small size of the optical elements which are on the tens of micrometer scale.

2. Experimental setup and methods

Here, we introduce a double-frequency Ronchi interferometry setup that is ideally targeted at measuring wavefront aberrations of microoptical elements and fulfils the aforementioned conditions. To obtain a large-size, wavefront-covering interferogram, we utilize a double-frequency Ronchi-grating (see Fig. 1) which features two similar spatial frequencies that cause two diffracted images that nearly lie on top of each other. This corresponds to a spatial shear of two wavefronts. The Ronchi interferogram is recorded and yields the lateral wavefront gradient $dW(x,y)/dx$. By rotating the grating by 90° or by using a crossed double-frequency grating, it is possible to record four interferograms simultaneously [35,36], where two of them contain also $dW(x,y)/dy$. By shifting the grating, it is possible to perform phase-shift interferometry with 5 or more steps, which allows for analytical retrieval and phase-unwrapping of the phase fronts [37–39].

The Ronchi grating is simply placed right at or close to the focal distance, modifying the fringe spatial frequency. Choosing the right z-distance between the microoptical element and the Ronchi grating allows for tuning the fringe spacing such that reliable phase retrieval is accomplished. This depends on the size of the image and the camera pixels. We typically record about 20–60 fringes across the entire field of view.

The Ronchi grating is then placed either behind a 3D printed micro-optical element that is printed onto a glass slide or onto a single-mode optical fiber. Laser illumination from a He-Ne laser at 633 nm which is expanded and refocused in an 80–200 mm zoom objective or from a fiber-coupled single mode laser diode at 658 nm is utilized (see Fig. 1(a) and (b)).

Figure 1(c) displays schematically the double-frequency Ronchi grating design: 50 nm thick chromium layers are deposited on a glass slide. Photoresist has been structured by electron beam lithography (grating sizes $500 \times 500 \mu\text{m}^2$ or $1 \times 1 \text{mm}^2$) of double-layer PMMA. After electron exposure and development, the chromium was evaporated by electron-beam evaporation, and a lift-off has been performed. The two gratings with grating periods g_1 and g_2 and 25% duty cycles each are added up and the values are limited to 100% absorption. Figure 1(d) depicts an SEM image of the fabricated double-frequency Ronchi grating, and the superperiod p with $1/p = 1/g_1 - 1/g_2$ is clearly visible.

The 3D printed microlenses which we analyzed in this paper were printed with commercially available photoresists, IP-S and IP-Dip (Nanoscribe), which exhibit a refractive index of 1.52, similar to glass [10]. The scanning speed, slicing and hatching parameters for the 3D printed lenses on fibers are 25,000 $\mu\text{m/s}$, 0.20 μm , and 0.15 μm , respectively.

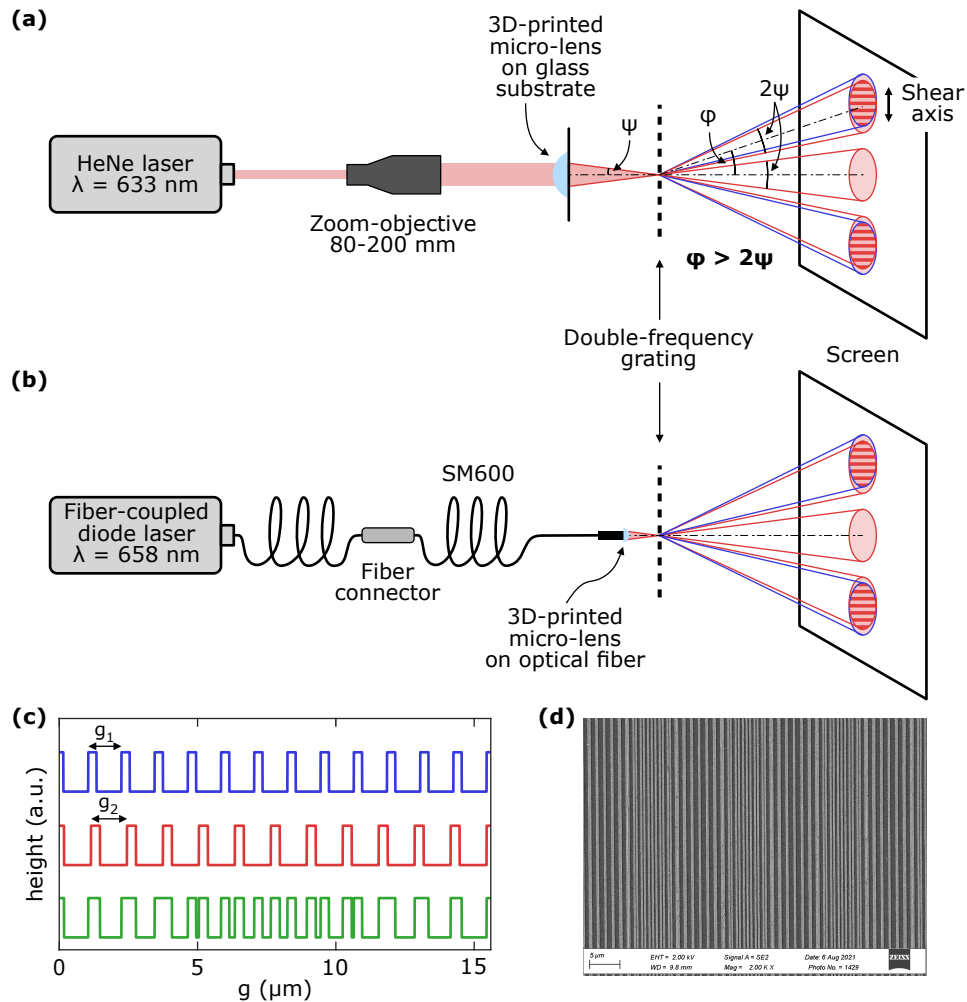


Fig. 1. (a) Ronchi interferometry setup for 3D printed microlenses: A HeNe laser is expanded in a 80–200 mm Zoom objective to a beam diameter in the mm range for optimal illumination of the microlenses. The 3D printed microlens focuses the beam, and a dual-frequency Ronchi transmission grating is placed near the focal plane with a small displacement in z -direction. A scattering screen and a camera record the 1st order spatial interferograms. The dual frequency grating yields sheared wavefronts which gives 1st diffraction order interferograms. (b) To characterize the wavefront of the microoptical element directly printed onto the single mode fiber (SM600), a fiber-coupled diode laser at 658 nm wavelength is coupled into the fiber. The Ronchi dual grating setup is the same as in (a). (c) Schematic height profile of the dual frequency Ronchi grating with 50 nm thickness of chromium on glass, with $g_1 = 1.2 \mu\text{m}$ and $g_2 = 1.3 \mu\text{m}$ periodicity and 25:75 metal:air duty cycle each. The two structures (blue and red) are added to yield the sum structure (green, rounded to 100% absorption) at the bottom of the figure. This structure is being manufactured by electron beam lithography into a $500 \times 500 \mu\text{m}^2$ patch. (d) SEM image of the manufactured dual-frequency grating. The superlattice beating period p with $1/p = 1/g_1 - 1/g_2$ is clearly visible.

3. Results and discussion

Figure 2(a) depicts microscope images (Keyence VHX-6000) of 3D printed microlenses. A Nanoscribe Quantum X printer with gray scale two-photon lithography was utilized which should give extremely smooth surfaces. A 25x microscope objective and 100 nm hatching distance was used to polymerize IP-S resist on a 700 μm thick glass slide. The lens shape had a ROC of 450 μm and a diameter of 450 μm . It was designed in an aspherical fashion with $f = 750 \mu\text{m}$ and an f -number of 1.65 ($\text{NA} = 0.3$). The design parameters are given in the Supplement 1. The lenses were illuminated through the glass, and the metal layer of the Ronchi grating faced the lenses. Images of the transmitted mode without (Fig. 2(b)) and with (Fig. 2(c)) the Ronchi grating have been recorded using a scattering screen. We set the z value of the Ronchi grating such that about 20 fringes were visible over the entire field of view.

The recorded Ronchi interferogram exhibits very evenly spaced, straight fringes, which is already indicative of quite low transversal wavefront aberrations. The Ronchi interferogram at $\lambda = 633 \text{ nm}$ was evaluated using the open source software DFT fringe [40]. This allowed to select the region of interest on the interferogram, which we picked to be about 350 μm in diameter.

Figures 2(d) and 2(e) display the retrieved wavefronts. The peak-to-peak aberration is about $\lambda/10$, and the RMS aberration is $0.047 \lambda \approx \lambda/20$, which is an excellent value for this supposedly ideal lens. Its Strehl ratio was 0.915, which confirms this assessment. Figure 2(f)–(h) plot the through-focus point spread function (PSF) for z -values of 10λ , 0 , $+10 \lambda$. Nearly diffraction limited performance with a close to perfect focal spot is visible particularly in Fig. 2(g).

Figures 2(i) and (j) plot the PSF of the lens as a function of the field and the MTF of the lens as a function of spatial frequency. These plots also confirm the close to diffraction limit performance. Table 2(k) lists the retrieved values for the Zernike polynomials, and the small values (all below 0.1) prove the excellent performance. We should mention that our results were very reproducible for the other lenses as well which were printed with the same printing parameters. They had similar Ronchi interferograms and wavefront aberration values.

For each lens design, several different interferograms of the same lens, as well as interferograms of different lenses printed with the same design, are taken and compared to investigate the excellent repeatability. We include some of the interferometry reports in the Supplement 1. Two different interferograms of the same lens, i.e., the aspherical perfect lens on glass depicted in Fig. 2, yield Strehl ratios of 0.914 and 0.915. The same lens design is used for several measurements.

Figure 3(a) depicts the Keyence microscope image of a 3D printed aspherical microlens on a single mode SM600 fiber with a 125 μm diameter no-core piece of 450 μm length with diameter 125 μm and a radius of curvature of 100 μm with an aspherical surface. A Nanoscribe GT using two-photon lithography mode printed the lens directly onto the fiber tip [41]. A 63x microscope objective and 200 nm hatching distance was used to polymerize IP-Dip resist directly on the fiber. The lenses were illuminated through the fiber using a single-mode fiber-coupled laser diode at $\lambda = 658 \text{ nm}$, and the metal layer of the Ronchi grating faced the lens. Images of the transmitted mode without (Fig. 3(b)) and with (Fig. 3(c)) the Ronchi grating have been recorded using a scattering screen. Again, we set the z value of the Ronchi grating such that about 20 fringes were visible over the entire field of view. The far field image of the mode (Fig. 3(b)) looks more or less perfectly Gaussian.

The recorded Ronchi interferogram exhibits once more very evenly spaced, straight fringes, which is already indicative of quite low transversal wavefront aberrations. Compared to Fig. 2(c), the fringes look even smoother, without much high-frequency noise. The Ronchi interferogram at $\lambda = 658 \text{ nm}$ was again evaluated using the open source software DFT fringe, and we selected a region of interest on the interferogram of about 120 μm in diameter.

Figures 3(d) and 3(e) display the retrieved wavefronts. The peak-to-peak aberration is about $\lambda/10$, and the RMS aberration is $0.046 \lambda \approx \lambda/20$, which is an excellent value for this supposedly

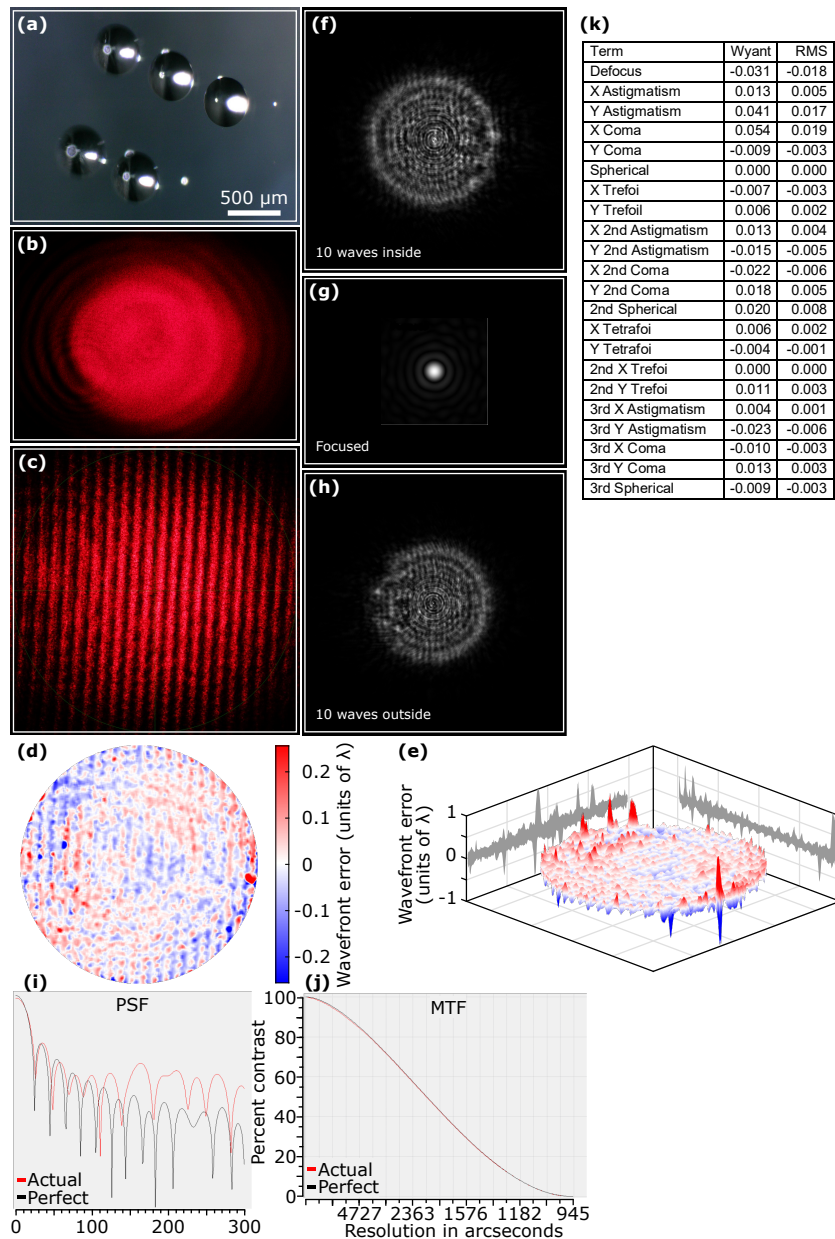


Fig. 2. (a) Keyence microscope image of 3D printed aspherical microlenses made from IP-S resist on a 700 μm thick glass substrate, diameter 450 μm , ROC = 450 μm , aspherical surface. The microlenses have been printed with the Nanoscribe Quantum X printer using gray scale two-photon lithography with a 25x objective. (b) Far field mode image of the laser beam far behind the focus. (c) Dual frequency 1st diffraction order Ronchi interferogram at $\lambda = 633 \text{ nm}$. (d) Retrieved wavefront. (e) 3D plot of the retrieved wavefront across a 370 μm field of view. The maximum wavefront aberration is $\pm 0.1 \lambda$, the RMS wavefront aberration is 0.047λ . (f), (g), (h): Through focus PSF (-10λ , 0 , $+10 \lambda$). A nearly diffraction limited focus is visible in (g). (i) Point spread function of the 3D printed microlens, which shows nearly diffraction limited performance up to very high fields. (j) Modulation transfer function (MTF), which indicates nearly diffraction limited performance, even for very high spatial frequencies (i.e. small resolution angles). Table (k) displays the retrieved values for the Zernike polynomials.

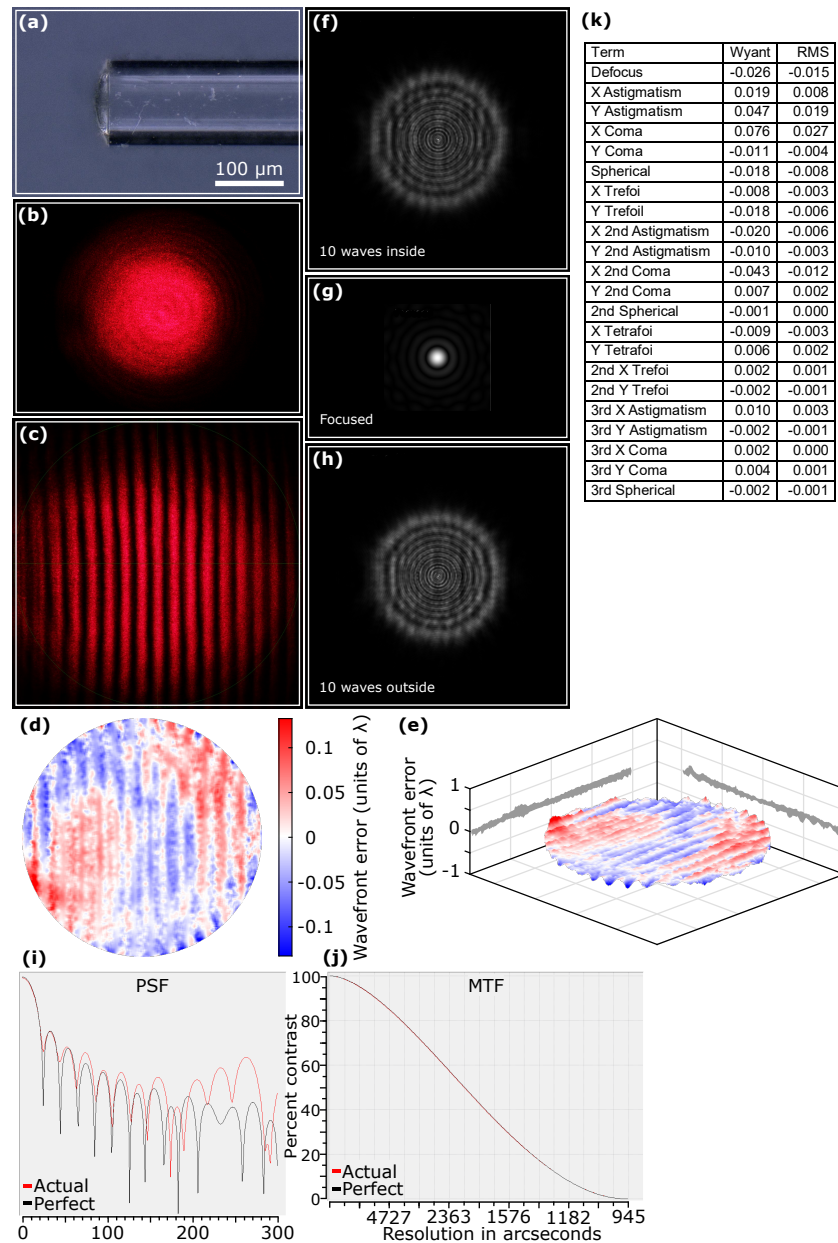


Fig. 3. (a) Keyence microscope image of a 3D printed aspherical microlens on a single mode SM600 fiber with a 125 μm diameter no-core piece of 450 μm length, diameter 125 μm , ROC = 100 μm , aspherical surface. The microlens from resist IP-Dip has been printed with the Nanoscribe GT printer with a 63x objective. (b) Far field mode image of the laser beam far behind the focus. (c) Dual frequency 1st diffraction order Ronchi interferogram at $\lambda = 658 \text{ nm}$. (d) Retrieved wavefront. (e) 3D plot of the retrieved wavefront across a 120 μm field of view. The maximum wavefront aberration is $\pm 0.1 \lambda$, the RMS wavefront aberration is 0.046λ . (f), (g), (h): Through focus PSF (-10λ , 0 , $+10 \lambda$). A nearly diffraction limited focus is visible in (g). (i) Point spread function of the 3D printed microlens, which shows nearly diffraction limited performance up to very high fields. (j) Modulation transfer function (MTF), which indicates nearly diffraction limited performance, even for very high spatial frequencies. Table (k) displays the retrieved values for the Zernike polynomials.

ideal lens. Its Strehl ratio was 0.921, which confirms this assessment. Figures 3(f)–(h) plot the through-focus point spread function (PSF) for z -values of 10λ , 0 , $+10\lambda$. Nearly diffraction limited performance with a close to perfect focal spot is visible particularly in Fig. 3(g). Multiple interferograms of this perfect lens, 3D printed on the optical fiber, give Strehl ratios of 0.920, 0.922, and 0.921. Here, we varied the number of fringes visible in the interferogram and achieved similar compositions of the Zernike polynomials for each interferogram taken of the same lens. The interferometry reports are included in the [Supplement 1](#). This further proves the repeatability of our setup to measure the wavefront aberrations of 3D printed microlenses.

Figures 3(i) and (j) plot the PSF of the lens as a function of the field and the MTF of the lens as a function of spatial frequency. These plots also confirm the close to diffraction limit performance. Table 3(k) lists the retrieved values for the Zernike polynomials, and the small values (all below 0.1) prove the excellent performance. We should mention that our results were very reproducible for more of such perfect lenses printed onto single mode fibers. They all had similar Ronchi interferograms and wavefront aberration values. Some of our fibers suffered from splicing issues, meaning that the no-core piece was not exactly centrally spliced onto the single mode fiber. In these cases, the Ronchi interferogram displayed some stronger aberrations.

Figure 4(a) depicts the Keyence microscope image of a 3D printed aspherical microlens on a single mode SM600 fiber with a $125\mu\text{m}$ diameter no-core piece of $450\mu\text{m}$ length with diameter $125\mu\text{m}$ and a radius of curvature of $100\mu\text{m}$ with a spherical surface and with deliberately introduced spherical aberration of 1λ . Just like before, a 63x microscope objective and 200 nm hatching distance was used to polymerize IP-Dip resist directly on the fiber. Illumination and Ronchi interferometry were performed exactly as before. Images of the transmitted mode without (Fig. 4(b)) and with (Fig. 4(c)) the Ronchi grating have been recorded using a scattering screen. In contrast to the perfect lens on fiber of Fig. (3), our far field mode image displays already signs of aberrations as expected.

The recorded Ronchi interferogram exhibits aberrated fringes, which is already indicative of the spherical wavefront aberrations. Evaluation and region of interest of $120\mu\text{m}$ diameter was performed as for Fig. (3).

Figures 4(d) and 4(e) display the retrieved wavefronts. The peak-to-peak aberration ranges from about $-\lambda/2$ to $+\lambda/2$, and the RMS aberration is 0.243λ . Its Strehl ratio was 0, which confirms the *not* diffraction limited performance. Figures 4(f)–(h) plot the through-focus point spread function (PSF) for z -values of 10λ , 0 , $+10\lambda$. Strongly spherically aberrated performance with a focal spot with clear diffraction rings is visible particularly in Fig. 4(g).

Figures 4(i) and (j) plot the PSF of the lens as a function of the field and the MTF of the lens as a function of spatial frequency. These plots also confirm the bad performance of this lens due to spherical aberration. Especially the MTF drops down significantly already for small spatial frequencies. Table 3(k) lists the retrieved values for the Zernike polynomials, especially the large value for spherical aberration stands out.

Figure 5 compares a side-looking OCT lens on a SM600 single mode fiber with a $125\mu\text{m}$ diameter no-core piece of $450\mu\text{m}$ length with a side-looking OCT lens on a SM600 single mode fiber *without* the no-core piece. Both lenses were printed with IP-S on a Nanoscribe GT with a 25x objective and 100 nm slicing distance. The reason was that IP-S is not as much a high-resolution resist in comparison to IP-Dip, which was used in Fig. 3 and 4, in order to generate a smoother reflection and exit front surface. These values were obtained after extensive optimization of objective lens, resist, and writing parameters. Figures 5(a) + (f) illustrate a schematic of the light ray propagation in this side-looking OCT fiber system. Figures 5(b) + (g) depict Keyence microscope images (side view of the lens front) of the two different lenses without laser illumination. Figures 5(c) + (h) display Keyence microscope images (side view of the lens front) with 658 nm single mode fiber illumination turned on. The large spot size and hence the large field illumination due to the beam expansion in the no-core piece of the fiber is clearly

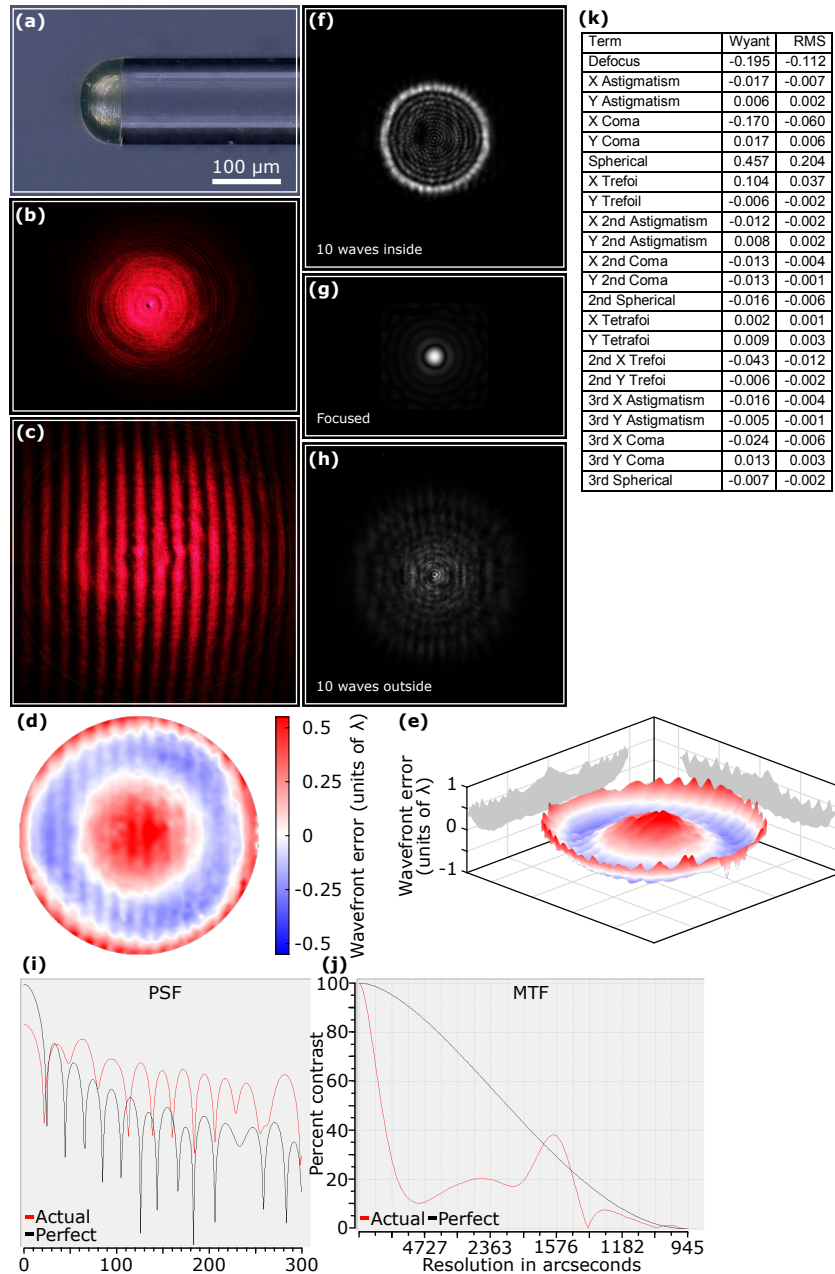


Fig. 4. (a) Keyence microscope image of a 3D printed aspherical *aberrated* microlens on a single mode SM600 fiber with a 125 μm diameter no-core piece of 450 μm length, diameter 125 μm , ROC = 100 μm , aspherical surface. The microlens from resist IP-Dip has been printed with the Nanoscribe GT printer with a 63x objective and has been deliberately designed with 1λ spherical aberration. (b) Far field mode image of the laser beam far behind the focus. (c) Dual frequency 1st diffraction order Ronchi interferogram at $\lambda = 658 \text{ nm}$. (d) Retrieved wavefront. (e) 3D plot of the retrieved wavefront across a 120 μm field of view. The maximum wavefront aberration is $\pm \lambda/2$, the RMS wavefront aberration is 0.243λ . The spherical aberration is nicely visible. (f), (g), (h): Through focus PSF (-10λ , 0 , $+10 \lambda$). A spherically aberrated focus is visible in (g). (i) Point spread function of the 3D printed microlens, which shows aberrated performance of the microlens. (j) Modulation transfer function (MTF), which indicates aberrated performance. Measured values exceeding the theoretical MTF are caused by artifacts in the data evaluation of highly aberrated lenses. Table (k) displays the retrieved values for the Zernike polynomials.

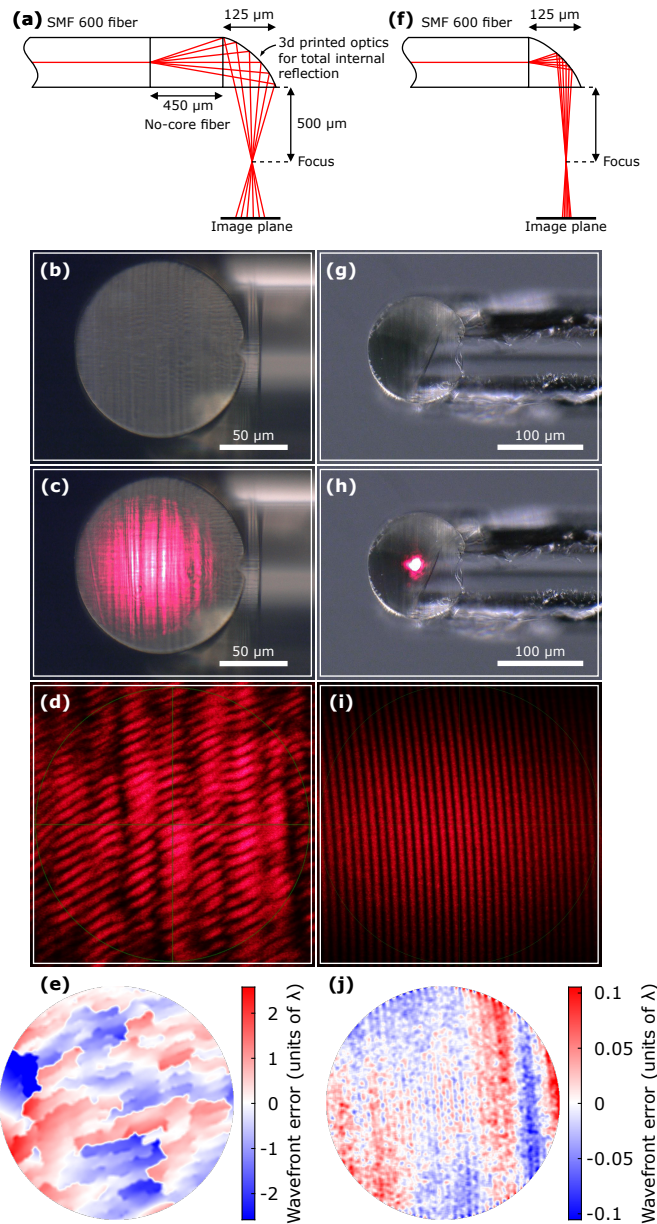


Fig. 5. (a)–(e): Side-looking OCT lens on a SM600 single mode fiber with a 125 μm diameter no-core piece of 450 μm length. (f)–(j): Side-looking OCT lens on a SM600 single mode fiber without the no-core piece. Both lenses were printed with IP-S on a Nanoscribe GT with a 25x objective and 100 nm slicing distance. (a) + (f) Schematic of the light ray propagation. (b) + (g): Keyence microscope images (side view of the lens front) of the two different lenses. (c) + (h): Keyence microscope images (side view of the lens front) with 658 nm single mode fiber illumination turned on. The large spot size and hence the large field illumination due to the beam expansion in the no-core piece of the fiber is clearly visible, in comparison to the rather small illuminated field in the fiber without the no-core piece. (d): Ronchi interferogram at $\lambda=658$ nm of the wavefront of the OCT lens printed onto the no-core fiber piece. A wavy structure due to the individually printed layers is clearly visible. (e) The retrieved wavefront indicates peak-to-peak aberrations from -1 to $+1 \lambda$. The RMS wavefront error is 0.493λ . (i) Ronchi interferogram of the OCT lens printed directly onto the SM600 fiber without the no-core piece. (j) The retrieved wavefront indicates much less aberrations of only $\pm \lambda/10$. The RMS wavefront error due to the much narrower and hence less sensitive illumination cone is 0.036λ .

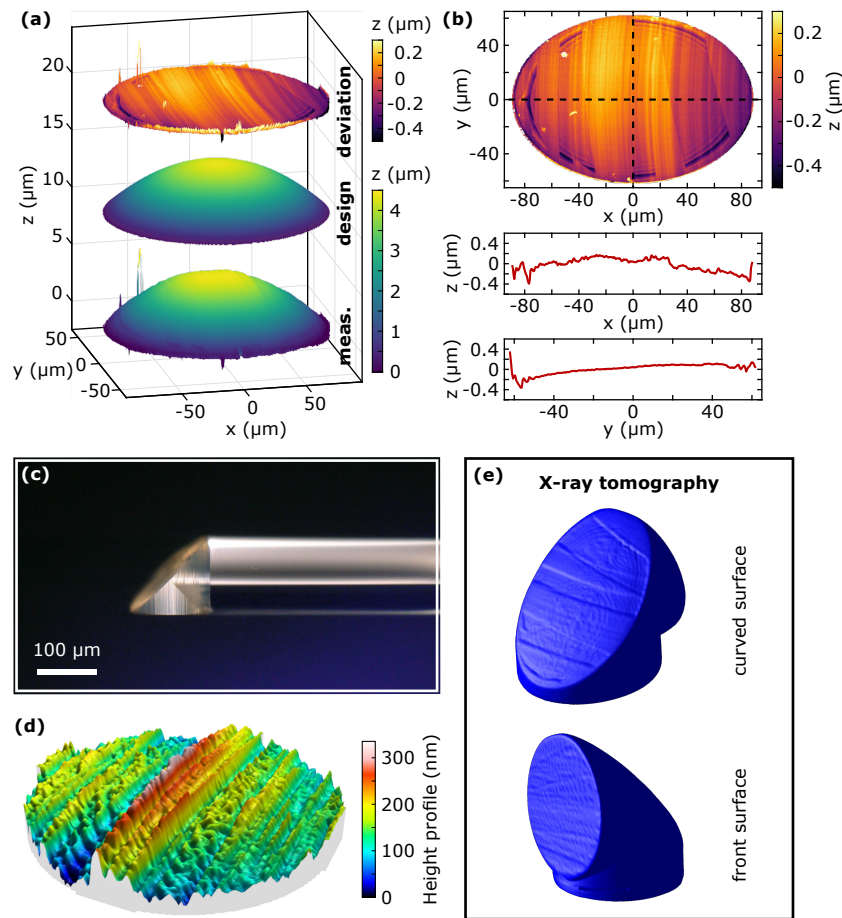


Fig. 6. (a) Nanofocus confocal measurement of the curved total internal reflection side of the OCT fiber printed onto the 450 μm long no-core fiber piece. The bottom image depicts the measurement, the center image is the design, and the top image depicts the difference between design and printed surface. (b) Deviation between design and measurement, and cross sections (indicated by dashed lines in the top figure) in x (middle figure) and y (bottom figure) direction. The peak deviations of the cross-section lie in the range below $\lambda/2$, while the peak deviation of the entire surface is 0.6 μm , which corresponds to 1λ . The evaluation of the RMS value of the surface roughness of the lens surface yields 20 nm. (c) Keyence microscope image of the side-looking OCT lens. The individually printed layers (slicing distance 100 nm) are clearly visible as vertical streaks in the image. (d) X-ray tomographic image of the total internal reflection side of the OCT lens. (e) Nanofocus confocal surface measurement of the front surface of the OCT lens (on the bottom side of figure (c)). The maximum deviation is in the range of $\lambda/2$. (f) X-ray tomographic image of the front side (beam exit) of the OCT lens.

visible, in comparison to the rather small illuminated field in the fiber without the no-core piece. Figure 5(d) reveals the Ronchi interferogram at $\lambda = 658\text{ nm}$ of the wavefront of the OCT lens printed onto the no-core fiber piece. A wavy structure due to the individually printed layers is clearly visible. The retrieved wavefront in Fig. 5(e) indicates aberrations from -1λ to $+1\lambda$. The RMS wavefront error is 0.493λ . The Ronchi interferogram of the OCT lens printed directly onto the SM600 fiber without the no-core piece is displayed in Fig. 5(i). The retrieved wavefront in

Fig. 5(j) indicates much less aberrations of only $\pm \lambda/10$. The RMS wavefront error due to the much narrower and hence less sensitive illumination cone is 0.036λ , and the Strehl ratio is 0.951. This indicates that the design of our side-looking optical OCT fiber works better without the no-core piece, however, probably at the expense of a changed beam waist, Rayleigh range, and numerical aperture.

In order to understand better the origin of the rather large aberrations of up to 1λ in the case of the OCT side-looking lens with the no-core fiber piece underneath, we examined more closely the 3D printed surfaces of the lens. Figure 6(a) presents a confocal surface measurement (Nanofocus profiler) of the curved total internal reflection side of the OCT fiber printed onto the no-core fiber piece. The bottom image depicts the measurement, the center image is the designed surface, and the top image displays the difference between designed and printed surface. Figure 6(b) plots the deviation between design and measurement, and cross sections (indicated by dashed lines in the top figure) in x (middle figure) and y (bottom figure) direction. The peak deviations of the cross-section lie in the range below $\lambda/2$, while the peak deviation of the entire surface is $0.6 \mu\text{m}$, which is one wavelength. The evaluation of the RMS value of the surface roughness of the lens surface gives 20 nm . Figure 6(c) shows a Keyence microscope image of the side-looking OCT lens. The individually printed layers (slicing distance 100 nm) are clearly visible as vertical streaks in the image. Figure 6(d) presents an X-ray tomographic image of the total internal reflection side of the OCT lens. Figure 6(e) depicts Nanofocus confocal surface measurements of the front surface of the OCT lens (on the bottom side of Fig. 6(c)). The maximum deviation is in the range of $\lambda/2$. Figure 6(f) exhibits the X-ray tomographic image of the front side (beam exit) of the OCT lens. It is clearly visible that the parallel printing plane (parallel to the fiber cleave) and the lateral slicing inaccuracy leads to some deviations, which cause the surface deviations. However, there are also other “streaks” going across the reflecting and exit surfaces, whose origins lie probably in manufacturing errors. We are currently trying to locate those manufacturing errors with the help of a combination of Keyence microscope images, Nanofocus confocal measurements, X-ray tomography, and Ronchi interferometry.

4. Conclusion

In conclusion, we have presented a suitable ultracompact interferometry method for 3D printed microoptics on glass substrates as well as for microoptics directly printed on fibers. We utilized double-frequency Ronchi interferometry to measure the actual wavefront aberrations of propagated light through such microoptics. The interferometric results confirm the extremely high quality of forward-looking 3D printed optical elements, which yield diffraction limited performance in the mid-visible range with Strehl ratios of over 0.95. Side-looking 3D printed OCT lenses on optical fibers that were illuminated over their entire numerical aperture with the aid of a no-core fiber piece on the single mode fiber suffered aberrations due to manufacturing streaks of up to 1λ . These aberrations could be reduced by illuminating the optical system without a no-core fiber piece.

In the future, a combination of Keyence microscope images, Nanofocus confocal measurements, X-ray tomography of the entire 3D microoptical systems, and Ronchi interferometry to quickly determine the actual wavefront aberrations of the optical system will provide a vast toolbox for error characterization of 3D printed microoptics. Especially our ultracompact Ronchi interferometry will provide a fast turnaround measurement process to iteratively optimize the 3D printing procedure in-line and in-situ. Its volume is small enough to be included on top or inside a Nanoscribe GT or Quantum X system, and the recording of the interferogram and the subsequent determination of the wavefront error takes only a few seconds. This will lead ultimately to extremely fast adjustments even for unknown designs in serial production of 3D printed microoptics and extremely high-quality yield even after the first few produced systems.

Funding. Bundesministerium für Bildung und Forschung (Printoptics); European Research Council (PoC Nr. 862549 3D Printedoptics); Baden-Württemberg Stiftung (Opterial); Bundesministerium für Wirtschaft und Klimaschutz (Exist und Junge Innovatoren); Ministerium für Wissenschaft, Forschung und Kunst Baden-Württemberg (ICM 5D printing).

Disclosures. The authors declare no conflicts of interest.

Data availability. Data underlying the results presented in this paper are not publicly available at this time but may be obtained from the authors upon reasonable request.

Supplemental document. See [Supplement 1](#) for supporting content.

References

1. H. B. Sun, S. Matsuo, and H. Misawa, "Three-dimensional photonic crystal structures achieved with two-photon-absorption photopolymerization of resin," *Appl. Phys. Lett.* **74**(6), 786–788 (1999).
2. M. Malinauskas, A. Žukauskas, S. Hasegawa, *et al.*, "Ultrafast laser processing of materials: from science to industry," *Light: Sci. Appl.* **5**(8), e16133 (2016).
3. P. Somers, A. Münchinger, S. Maruo, *et al.*, "The physics of 3D printing with light," *Nat. Rev. Phys.* **6**(2), 99–113 (2023).
4. G. V. Freymann, A. Ledermann, M. Thiel, *et al.*, "Three-Dimensional Nanostructures for Photonics," *Adv. Funct. Mater.* **20**(7), 1038–1052 (2010).
5. L. Siegle, S. Ristok, and H. Giessen, "Complex aspherical singlet and doublet microoptics by grayscale 3D printing," *Opt. Express* **31**(3), 4179–4189 (2023).
6. S. Ristok, S. Thiele, A. Toulouse, *et al.*, "Stitching-free 3D printing of millimeter-sized highly transparent spherical and aspherical optical components," *Opt. Mater. Express* **10**(10), 2370–2378 (2020).
7. M. Schmid and H. Giessen, "Stress-induced birefringence in 3D direct laser written micro-optics," *Opt. Lett.* **47**(22), 5789–5792 (2022).
8. M. Schmid, F. Sterl, S. Thiele, *et al.*, "3D printed hybrid refractive/diffractive achromat and apochromat for the visible wavelength range," *Opt. Lett.* **46**(10), 2485–2488 (2021).
9. A. Toulouse, S. Thiele, K. Hirzel, *et al.*, "High resolution femtosecond direct laser writing with wrapped lens," *Opt. Mater. Express* **12**(9), 3801–3809 (2022).
10. M. Schmid, D. Ludescher, and H. Giessen, "Optical properties of photoresists for femtosecond 3D printing: refractive index, extinction, luminescence-dose dependence, aging, heat treatment and comparison between 1-photon and 2-photon exposure," *Opt. Mater. Express* **9**(12), 4564–4577 (2019).
11. T. Gissibl, S. Wagner, J. Sykora, *et al.*, "Refractive index measurements of photo-resists for three-dimensional direct laser writing," *Opt. Mater. Express* **7**(7), 2293–2298 (2017).
12. A. Žukauskas, M. Malinauskas, C. Reinhardt, *et al.*, "Closely packed hexagonal conical microlens array fabricated by direct laser photopolymerization," *Appl. Opt.* **51**(21), 4995–5003 (2012).
13. D. Gonzalez-Hernandez, S. Varapnickas, A. Bertocini, *et al.*, "Micro-Optics 3D Printed via Multi-Photon Laser Lithography," *Adv. Opt. Mater.* **11**(1), 2201701 (2023).
14. I. V. A. K. Reddy, A. Bertocini, and C. Liberale, "3D-printed fiber-based zeroth- and high-order Bessel beam generator," *Optica* **9**(6), 645–651 (2022).
15. C. Liberale, G. Cojoc, P. Candeloro, *et al.*, "Micro-optics fabrication on top of optical fibers using two-photon lithography," *IEEE Photonics Technol. Lett.* **22**(7), 474–476 (2010).
16. S. Thiele, C. Pruss, A. M. Herkommer, *et al.*, "3D printed stacked diffractive microlenses," *Opt. Express* **27**(24), 35621–35630 (2019).
17. D. Schäffner, T. Preuschoff, S. Ristok, *et al.*, "Arrays of individually controllable optical tweezers based on 3D-printed microlens arrays," *Opt. Express* **28**(6), 8640–8645 (2020).
18. S. Thiele, T. Gissibl, H. Giessen, *et al.*, "Ultra-compact on-chip LED collimation optics by 3D femtosecond direct laser writing," *Opt. Lett.* **41**(13), 3029–3032 (2016).
19. B. Chen, D. Claus, D. Russ, *et al.*, "Generation of a high-resolution 3D-printed freeform collimator for VCSEL-based 3D-depth sensing," *Opt. Lett.* **45**(19), 5583–5586 (2020).
20. J. Schwab, K. Weber, J. Drozella, *et al.*, "Coupling light emission of single-photon sources into single-mode fibers: mode matching, coupling efficiencies, and thermo-optical effects," *Opt. Express* **30**(18), 32292–32305 (2022).
21. M. Sartison, K. Weber, S. Thiele, *et al.*, "3D printed micro-optics for quantum technology: Optimised coupling of single quantum dot emission into a single-mode fibre," *Light Adv. Manuf.* **2**(2), 103 (2021).
22. S. Schmidt, S. Thiele, A. Toulouse, *et al.*, "Tailored micro-optical freeform holograms for integrated complex beam shaping," *Optica* **7**(10), 1279–1286 (2020).
23. B. G. Assefa, T. Saastamoinen, J. Biskop, *et al.*, "3D printed plano-freeform optics for non-coherent discontinuous beam shaping," *Opt. Rev.* **25**(3), 456–462 (2018).
24. K. Weber, F. Hütt, S. Thiele, *et al.*, "Single mode fiber based delivery of OAM light by 3D direct laser writing," *Opt. Express* **25**(17), 19672–19679 (2017).
25. G. B. Wu, K. F. Chan, and C. H. Chan, "3-D Printed Terahertz Lens to Generate Higher Order Bessel Beams Carrying OAM," *IEEE Trans. Antennas Propagat.* **69**(6), 3399–3408 (2021).
26. L. Bremer, K. Weber, S. Fischbach, *et al.*, "Quantum dot single-photon emission coupled into single-mode fibers with 3D printed micro-objectives," *APL Photonics* **5**(10), 106101 (2020).

27. P. Ruchka, S. Hammer, M. Rockenhäuser, *et al.*, “Microscopic 3D printed optical tweezers for atomic quantum technology,” *Quantum Sci. Technol.* **7**(4), 045011 (2022).
28. A. Asadollahbaik, S. Thiele, K. Weber, *et al.*, “Highly Efficient Dual-Fiber Optical Trapping with 3D Printed Diffractive Fresnel Lenses,” *ACS Photonics* **7**(1), 88–97 (2020).
29. J. Li, P. Fejes, D. Lorensen, *et al.*, “Two-photon polymerisation 3D printed freeform micro-optics for optical coherence tomography fibre probes,” *Sci. Rep.* **8**(1), 14789 (2018).
30. J. Fischer, G. V. Freymann, and M. Wegener, “The Materials Challenge in Diffraction-Unlimited Direct-Laser-Writing Optical Lithography,” *Adv. Mater.* **22**(32), 3578–3582 (2010).
31. R. Zvagelsky, P. Kiefer, J. Weinacker, *et al.*, “In-situ Quantitative Phase Imaging during Multi-photon Laser Printing,” *ACS Photonics* **10**(8), 2901–2908 (2023).
32. J. Weinacker, S. Kalt, P. Kiefer, *et al.*, “On Iterative Pre-Compensation of 3D Laser-Printed Micro-Optical Components Using Confocal-Optical Microscopy,” *Adv. Funct. Mater.* **2309356**, 1 (2023).
33. R. Zvagelsky, F. Mayer, D. Beutel, *et al.*, “Towards in-situ diagnostics of multi-photon 3D laser printing using optical coherence tomography,” *Light: Advanced Manufacturing* **3**(3), 1 (2022).
34. D. Malacara, “*Optical shop testing*,” Wiley-Interscience, Hoboken, NY, 3rd. Edition (2007).
35. J. C. Wyant, “Double Frequency Grating Lateral Shear Interferometer,” *Appl. Opt.* **12**(9), 2057–2060 (1973).
36. J. C. Wyant and K. Creath, “Basic Wavefront Aberration Theory for Optical Metrology,” *Appl. Opt. a. opt. Eng.* (Academic Press 1992), Vol.9.
37. C. Ai and J. C. Wyant, “Effect of Spurious Reflection on Phase Shift Interferometry,” *Appl. Opt.* **27**(14), 3039–3045 (1988).
38. M. Takeda, H. Ina, and S. Kobayashi, “Fourier-transform method of fringe-pattern analysis for computer-based topography and interferometry,” *J. Opt. Soc. Am.* **72**(1), 156–161 (1982).
39. F. Wu, J. Han, and F. Tang, “Method for designing phase-retrieval algorithms for Ronchi phase-shifting lateral-shearing interferometry,” *Appl. Opt.* **58**(13), 3379 (2019).
40. <https://github.com/githubdoe/DFTFringe>, (2020).
41. T. Gissibl, S. Thiele, A. Herkommer, *et al.*, “Sub-micrometre accurate free-form optics by three-dimensional printing on single-mode fibres,” *Nat. Commun.* **7**(1), 11763 (2016).